ACCSCIENCE PUBLISHING

International Journal of Bioprinting

RESEARCH ARTICLE

Roughness-engineered 3D-printed microfluidics for continuous glucose and lactate sensing in 3D in vitro tissue models

Giheon Kim[1], Yeonghwa Hong[1], Seungjun Lee[1,2], Namsun Chou[2], and Hyogeun Shin[1,3]*

[1]School of Electronic and Electrical Engineering, College of IT Engineering, Kyungpook National University, Daegu, Republic of Korea

[2]Emotion, Cognition & Behavior Research Group, Korea Brain Research Institute (KBRI), Daegu, Republic of Korea

[3]Brain Science and Engineering Institute, Kyungpook National University, Daegu, Republic of Korea

Abstract

Monitoring metabolic flux in 3D tissue models is essential for validating physiological maturity and maintaining homeostatic balance. However, conventional optical-based analytical techniques often fail to capture dynamic and transient metabolic shifts due to phototoxicity, signal attenuation in thick 3D constructs, and the requirement for invasive labeling, all of which hinder long-term, continuous monitoring. Standard assays such as high-performance liquid chromatography (HPLC) and enzyme-linked immunosorbent assay (ELISA) are also inherently time-consuming and labor-intensive. Although electrochemical sensors offer a promising alternative, their integration into microfluidic platforms is frequently constrained by limited mass transport and the poor scalability of traditional lithography-based fabrication methods. Herein, we report an integrated, roughness-engineered microfluidic platform that addresses these limitations by strategically exploiting the "stair-stepping" artifacts inherent to fused deposition modeling (FDM) 3D printing as functional passive micromixers. By repurposing these manufacturing defects into deterministic micro-topographies, the platform induces chaotic advection, disrupting the boundary layer and enhancing solute exchange at physiologically relevant low flow rates. Numerical simulations elucidate the correlation between surface roughness and fluidic vorticity, providing a robust framework for performance optimization. Experimental validation demonstrates superior sensitivity, with a glucose response of 6.983 nA/mM and a lactate response of 5.669 nA/mM. Finally, real-time monitoring of biomimetic hydrogel phantoms over 500 min underscores the platform's potential as a scalable and cost-effective quality control tool for 3D *in vitro* tissue engineering and regenerative medicine.

Keywords: 3D printing; Metabolic monitoring; Microfluidics; Topographical engineering; Fused deposition modeling

***Corresponding author:**
Hyogeun Shin
(hyogeunshin@knu.ac.kr)

Citation: Kim G, Hong Y, Lee S, Chou N, Shin H. Roughness-engineered 3D-printed microfluidics for continuous glucose and lactate sensing in 3D in vitro tissue models. *Int J Bioprint.* 2026:12(2):026050045. doi: 10.36922/IJB026050045

Received: February 1, 2026

Revised: March 11, 2026

Accepted: March 12, 2026

Published online: April 14, 2026

1. Introduction

The development of functional 3D *in vitro* tissue models that accurately recapitulate human physiology is a central goal in tissue engineering and regenerative medicine.[1,2] As these models, such as spheroids and organoids, evolve from simple structural assemblies into functionally mature living systems, continuous monitoring of metabolic flux becomes critical for maintaining homeostasis and validating physiological relevance.[3] Metabolic activity serves as a real-time indicator of cellular health, offering immediate feedback on nutrient uptake and pathological shifts.[4,5] In particular, glucose consumption and lactate production are key metabolic indicators, as changes in their levels reflect the balance between oxidative phosphorylation and anaerobic glycolysis.[6] Although optical assessment techniques (*e.g.*, fluorescence imaging and pH-sensitive dyes) offer high spatial resolution, they often suffer from phototoxicity and signal attenuation in thick 3D constructs, as well as require invasive labeling, which hinders long-term, continuous monitoring.[7–9] Furthermore, conventional metabolic analyses predominantly rely on discrete off-line assays (*e.g.*, high-performance liquid chromatography [HPLC], enzyme-linked immunosorbent assay [ELISA], or colorimetric enzymatic kits), which are time-consuming and incapable of capturing the dynamic, transient metabolic shifts inherent in living systems.

To address these limitations, electrochemical sensing offers a promising label-free alternative with superior temporal resolution.[10,11] However, to fully realize its potential within the 3D *in vitro* tissue models, these sensors must be seamlessly integrated into advanced microfluidic platforms capable of precisely managing nutrient perfusion and collecting metabolic byproducts, thereby enabling accurate spatiotemporal monitoring of the cellular microenvironment.[12,13] The performance of such integrated electrochemical systems is fundamentally governed by mass transport dynamics within the microfluidic channel. Sensitivity and response time are frequently constrained by the formation of a stagnant boundary layer at the electrode surface, where slow molecular diffusion becomes the rate-limiting step. To overcome these transport limitations, integrated microfluidic platforms have been developed to enhance in situ mass transport and enable precise fluid delivery.[14] For these systems to be viable within 3D tissue-on-a-chip platforms, they must provide rapid response times and high sensitivity, even under low flow rates (<100 μL/min) typical of physiological conditions. Nevertheless, widespread adoption remains limited by traditional lithography-based fabrication methods, which restrict scalability and cost-efficiency.[15]

Additive manufacturing, particularly 3D printing, has emerged as a disruptive technology that enables rapid and cost-effective prototyping of complex microfluidic architectures.[16] While high-resolution modalities such as vat photopolymerization have been increasingly refined through advanced optimization—including machine learning-based approaches to achieve superior dimensional fidelity in microfluidic components[17]—fused deposition modeling (FDM) is widely employed due to its accessibility and material versatility.[18,19] However, FDM-printed components inherently exhibit a distinct surface morphology, referred to as the 'stair-stepping' effect, resulting from the layer-by-layer deposition of thermoplastic filaments.[20–22] While this intrinsic surface roughness (R_a) is traditionally regarded as a manufacturing defect that disrupts predictable laminar flow, we propose a paradigm shift by strategically repurposing this micro-topography as a functional passive micromixer. Specifically, the programmed nozzle path generates periodic microstructures that induce chaotic advection, effectively disrupting the stagnant boundary layer and enhancing solute exchange at the electrochemical interface. In this study, we employ comprehensive numerical simulations to elucidate the physical correlations among surface roughness (R_a), fluidic vorticity, and Péclet number (P_e), establishing a robust framework for optimizing mass transport under physiologically relevant low-flow conditions.

Herein, we present the development of an integrated, FDM-derived microfluidic sensing platform for the simultaneous and non-invasive monitoring of glucose and lactate *in vitro*. By synergistically combining the engineered surface roughness of FDM-printed molds with a serpentine channel architecture, we demonstrate a substantial enhancement in electrochemical sensing performance. Numerical simulations and experimental validation collectively confirm that the chaotic advection induced by the micro-topographical features reduces boundary-layer thickness, resulting in superior sensitivity and faster response times compared to smooth-channel counterparts. To further validate the physiological relevance of our platform within 3D tissue-on-a-chip, we employed biomimetic hydrogel tissue phantoms to emulate the dynamic metabolic release profiles of engineered tissues. The platform's ability to resolve transient concentration shifts at high temporal resolution underscores its potential as a scalable, cost-effective quality-control tool for bioreactors and regenerative medicine. This work offers a practical yet robust strategy for integrating real-time metabolic flux analysis into 3D *in vitro* tissue models.

2. Materials and methods

2.1. Materials

For the fabrication of the microfluidic master molds, poly(lactic acid) (PLA) filaments (K1 Max, Creality, China) were employed in FDM to generate engineered rough surfaces, whereas a white photopolymer resin (Form 4B, Formlabs, USA) was used in stereolithography (SLA) to fabricate smooth-surfaced control molds. Chlorotrimethylsilane and hexane were obtained from Sigma-Aldrich (USA) to clearly demold polydimethylsiloxane (PDMS) from the fabricated master molds. *D*-(+)-glucose and sodium *L*-lactate, used for electrochemical sensing evaluations, were procured from Sigma-Aldrich (USA). To synthesize the biomimetic 3D hydrogel tissue phantoms, sodium alginate and calcium chloride ($CaCl_2$) were also obtained from Sigma-Aldrich (USA) and used as received without further purification. All aqueous solutions were prepared using deionized water and phosphate-buffered saline (PBS, pH 7.4) to maintain physiologically relevant conditions during electrochemical testing.

2.2. Fabrication and patterning of electrochemical electrodes

The electrochemical electrodes, including a working electrode (WE), counter electrode (CE), and reference electrode (RE), were patterned on a 4-inch glass wafer. The wafer was initially cleaned with acetone and rinsed with deionized water to remove organic contaminants. A negative photoresist (DNR 21.8 cp) was then spin-coated onto the wafer to define the electrode geometries, followed by ultraviolet (UV) exposure. Subsequently, a 50-nm-thick titanium (Ti) adhesion layer and a 100-nm-thick gold (Au) layer were sequentially deposited via electron-beam evaporation (SRN-200, SORONA, Korea). To passivate the signal lines and electrode surfaces while defining the active sensing regions, a second photoresist layer (positive PR; GXR-601) was spin-coated. A 50-nm-thick SiO_2 insulation layer was then deposited across the entire wafer. Following lift-off, only the designated active areas of the WE, CE, and RE remained exposed for sensing applications.

2.3. Enzyme immobilization on electrochemical electrodes

Enzyme immobilization was conducted on the exposed active areas of the Au WEs using a modified covalent functionalization protocol. The electrode surfaces were first activated via 1-ethyl-3-(3-dimethylaminopropyl) carbodiimide hydrochloride (EDC)/N-hydroxysuccinimide (NHS) chemistry to promote stable enzyme attachment. Specifically, the fabricated electrochemical electrodes were incubated in an activation solution containing 16.2 mM EDC and 80 mM NHS in 1 M PBS at room temperature for 30 min.

Following activation, the electrodes were rinsed with deionized water to remove residual reagents. Enzymes were then immobilized by applying droplets of 2 mg/mL glucose oxidase (GOx) and 2 mg/mL lactate oxidase (LOx), each dissolved in PBS, onto the respective WEs. The immobilization was carried out at 4 °C for 12 h to preserve enzymatic activity. Unbound enzymes were subsequently removed by rinsing with PBS. The functionalized electrode chips were stored under humidified conditions at 4 °C until integration into the microfluidic device.

2.4. Fabrication of PDMS microfluidic channel

Microfluidic channels were fabricated using 3D-printed master molds, and prepared by two methods—FDM for rough surfaces and SLA for smooth surfaces—to investigate the effect of surface topography on mixing efficiency. Prior to PDMS casting, the master molds were immersed in a silanizing solution—a mixture of chlorotrimethylsilane and hexane—for 30 min to ensure clean demolding and preventing the formation of surface defects. A PDMS prepolymer was mixed with a curing agent at a 10:1 weight ratio, then poured into the molds and cured in an oven at 80 °C for 2 h.

After curing, the PDMS replicas were carefully demolded, and inlet/outlet ports were created using a 0.75 mm biopsy punch. Both the patterned PDMS and a clean glass wafer substrate were treated with oxygen plasma (PS-100, Korea) at 40 W for 30 s and subsequently bonded. The assembled device was then placed in an oven at 80 °C for 1 h to enhance bonding strength.

2.5. Surface characterization of 3D-printed molds

The surface morphology and topography of the FDM- and SLA-printed molds were characterized prior to PDMS replication to verify engineered roughness. Scanning electron microscopy (SEM; EM-30, Korea) was used to visualize microscale features, while surface roughness was quantitatively assessed using a stylus profilometer (Alpha-step D-600, KLA, USA). Measurements of average surface roughness (R_a) and cross-sectional height profiles were performed along a direction perpendicular to the filament deposition path.

2.6. Evaluation of electrochemical sensitivity and selectivity

Prior to assessing sensing capabilities, the electrical performance of the electrochemical electrodes was evaluated using cyclic voltammetry (CV) with a

potentiostat (PalmSense4, Netherlands). CV scans were performed in 1 M PBS (pH 7.0), ranging from −1.0 V to +1.0 V for bare Au electrodes and from −0.8 V to +0.8 V for enzyme-immobilized electrodes, at scan rates of 20, 50, 100, 200, 500, and 1000 mV/s.

Sensing performance was characterized by chronoamperometry in 0.1 M PBS (pH 7.0) at room temperature under an applied potential of +0.1 V. Glucose and lactate were sequentially introduced at concentrations of 0.2, 0.5, 1.0, 2.0, and 4.0 mM using a syringe pump. Selectivity was assessed under the same conditions using 1 mM ascorbic acid (AA) and uric acid (UA) as potential interfering species.

2.7. Preparation and characterization of biomimetic 3D tissue hydrogel phantoms

To simulate the release of metabolic byproducts from 3D *in vitro* tissue constructs, spherical hydrogel phantoms were fabricated by encapsulating metabolic analytes within an alginate matrix. A 2.0% (*w*/*v*) sodium alginate solution was prepared by dissolving alginate powder in deionized water under vigorous stirring. *D*-(+)-glucose (10 mM) and *L*-lactate (5 mM) were added to the solution and homogenized to mimic the internal metabolite concentrations.

The resulting mixture was loaded into a syringe fitted with a 23 G microneedle and extruded dropwise into a 100 mM $CaCl_2$ crosslinking bath. The phantoms were incubated in the bath for 30 min to ensure complete gelation, then rinsed with deionized water to remove excess calcium ions and surface-bound analytes. Morphology and average diameter (~0.5 mm) were assessed using optical microscopy to confirm uniformity and compatibility with the microfluidic channel dimensions.

2.8. Statistical analysis

The statistical analyses were performed using GraphPad Prism (GraphPad, USA). The specific statistical analysis methods used for each dataset is indicated in the corresponding figure legend, where applicable.

3. Results and discussion

3.1. Design and physical characterization of roughness-engineered molds

The integrated fabrication strategy enables effective mixing without relying on predefined microfluidic architectures, such as herringbone patterns,[23] by leveraging the inherent surface artifacts produced by 3D printing. This approach enables rapid prototyping and the intentional introduction of surface roughness without requiring complex cleanroom-based lithography (Figure 1). To validate the fidelity of the engineered topography, the surface morphology of the 3D-printed master molds was examined using SEM and stylus profilometry (Figure 2). The SLA-printed mold served as a smooth control, exhibiting a nearly featureless, isotropic surface profile (Figure 2a). In contrast, FDM-printed molds displayed a distinct periodic topography arising from the stair-stepping effect, an inherent artifact of the layer-by-layer filament deposition process. The structural integrity of these layer lines and their internal geometry were consistently maintained, as evidenced by the cross-sectional analysis of the master mold, resulting in a well-defined anisotropic roughness (Figure S1). Notably, molds printed with a 0.4 mm layer height exhibited more prominent and wider ridges than those printed at 0.2 mm, indicating that the degree of passive mixing can be tuned by adjusting FDM printing parameters.

The three-dimensional complexity of the engineered surfaces was further evident from alternative viewing angles (Figure 2b). While the SLA surface remained flat even under inclined observation, FDM molds revealed a pronounced anisotropic relief consisting of alternating ridges and grooves. This engineered roughness provides the structural foundation for inducing passive mixing within the microchannel. In the 0.4 mm FDM model, height variations appeared as deep, well-defined troughs between adjacent filament layers. This morphology is designed to function as a series of micro-obstacles that disrupt laminar flow streamlines, thereby enhancing analyte transport from the bulk flow toward the electrode surface.

Quantitative validation of these surface profiles was obtained using Alpha-step stylus profilometry (Figure 2c). The Z-axis profile across a 2.0 mm scan length confirmed the marked differences in topographical amplitude among the three groups. The SLA mold (black line) exhibited baseline-level roughness with negligible fluctuations, confirming its role as a smooth control. In contrast, the FDM 0.2 mm mold (red line) displayed periodic oscillations with a peak-to-valley height of approximately 5 μm, while the FDM 0.4 mm mold (blue line) exhibited significantly greater topographical complexity, characterized by irregular yet periodic peaks reaching heights of 20–25 μm. This quantitative increase in surface roughness (R_a) presents a substantial barrier, inducing the fluidic vorticity necessary for high-sensitivity detection in electrochemical sensors.

To confirm that these engineered features were successfully transferred to the final microfluidic device, the replication fidelity of the PDMS channels was rigorously validated. Through the SEM images, the micro-topographical features were faithfully transferred to the PDMS inner walls without observable tearing or structural

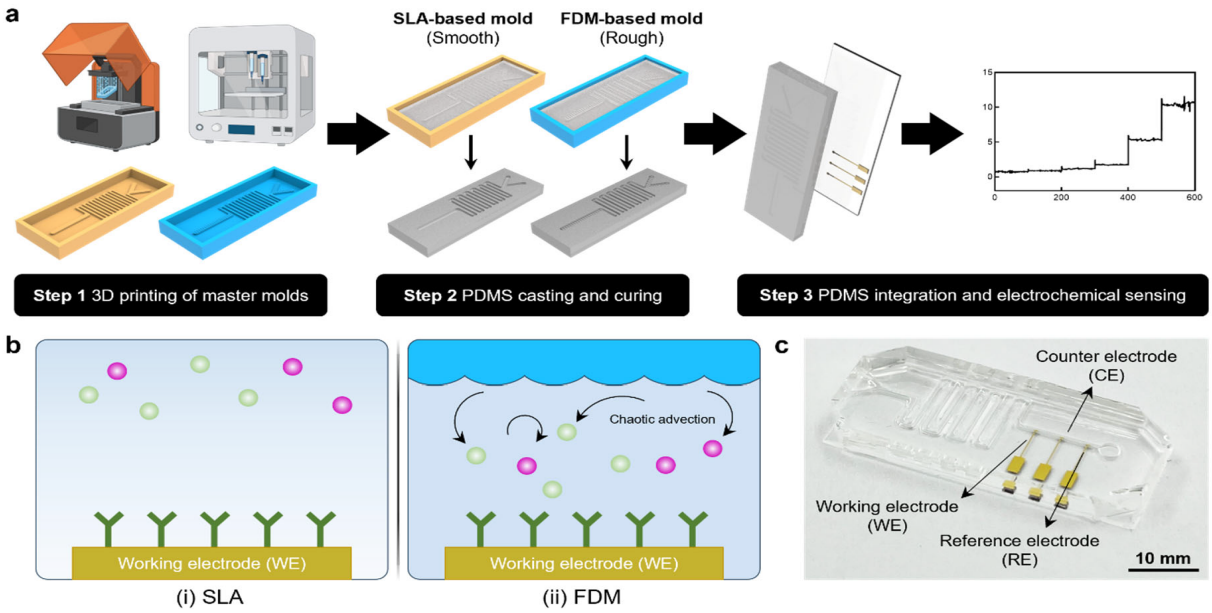

Figure 1. Overview of the integrated fabrication workflow, sensing mechanism, and physical characterization of the microfluidic sensing platform. (a) Step-by-step schematic illustration of the fabrication process: Step 1 shows the 3D printing of master molds using SLA (smooth) and FDM (rough) techniques; Step 2 depicts the PDMS casting and demolding process; and Step 3 shows the final integration of the microfluidic channel with electrochemical sensors for real-time monitoring. (b) Conceptual comparison of mass transport mechanisms at the sensing interface: (i) Diffusion-limited sensing in SLA-based channels with smooth surfaces versus (ii) enhanced mass transport through chaotic advection induced by the deterministic FDM micro-topography. (c) Optical photograph of the fully assembled microfluidic device, highlighting the integrated three-electrode system (working electrode, WE; reference electrode, RE; counter electrode, CE) and the serpentine channel geometry.
Abbreviations: FDM: Fused deposition modeling; PDMS: Polydimethylsiloxane; SLA: Stereolithography.

defects (Figure S2). Quantitative surface profiling of the PDMS replicates further confirmed that the replicated PDMS maintained a peak-to-valley height of 20–25 μm, demonstrating high-fidelity replication of the topography of the master molds (Figure S3).

Furthermore, the dimensional fidelity of the fabrication process was assessed to eliminate unintended geometric variables across different printing modalities (Table S1). The dimensional error for the FDM-based PDMS channels was less than 1.12% compared to the CAD design, and the size difference between the SLA and FDM groups was negligible. These results demonstrate that the subsequent sensing enhancements are fundamentally attributed to the engineered roughness rather than variations in channel cross-sectional area.

3.2. Numerical simulation and experimental validation of fluid mixing mechanisms

To elucidate the physical mechanism underlying the enhanced sensing performance, comprehensive numerical simulations and dye-mixing experiments were conducted to visualize fluid dynamics across microchannel configurations (Figure 3). The serpentine microchannel was modeled to assess how engineered surface roughness affects mixing efficiency under a flow rate of 100 μL/min (Figure 3a). Velocity profile simulations revealed a distinct transition in flow regimes as a function of surface topography (Figure 3b). In the SLA-based smooth channel, the fluid exhibited a characteristic parabolic velocity profile, with a localized high-velocity core and substantial stagnant zones near the channel boundaries. Although the FDM 0.2 mm channel showed slight expansion of the flow field, it remained predominantly laminar. By contrast, the FDM 0.4 mm channel demonstrated a broad redistribution of velocity across the entire cross-section. The rough-surface ridges redirected momentum toward the channel walls, thereby disrupting the stagnant boundary layer that typically impedes mass transport at the electrode interface.

This hydrodynamic perturbation was directly reflected in the concentration gradient simulations (Figure 3c). In both the SLA and FDM 0.2 mm models, pronounced depletion zones formed near the bottom and side walls, indicating that analyte delivery was limited by slow molecular diffusion. However, the FDM 0.4 mm channel maintained a high, uniform concentration at the sensing interface. By inducing chaotic advection, the engineered

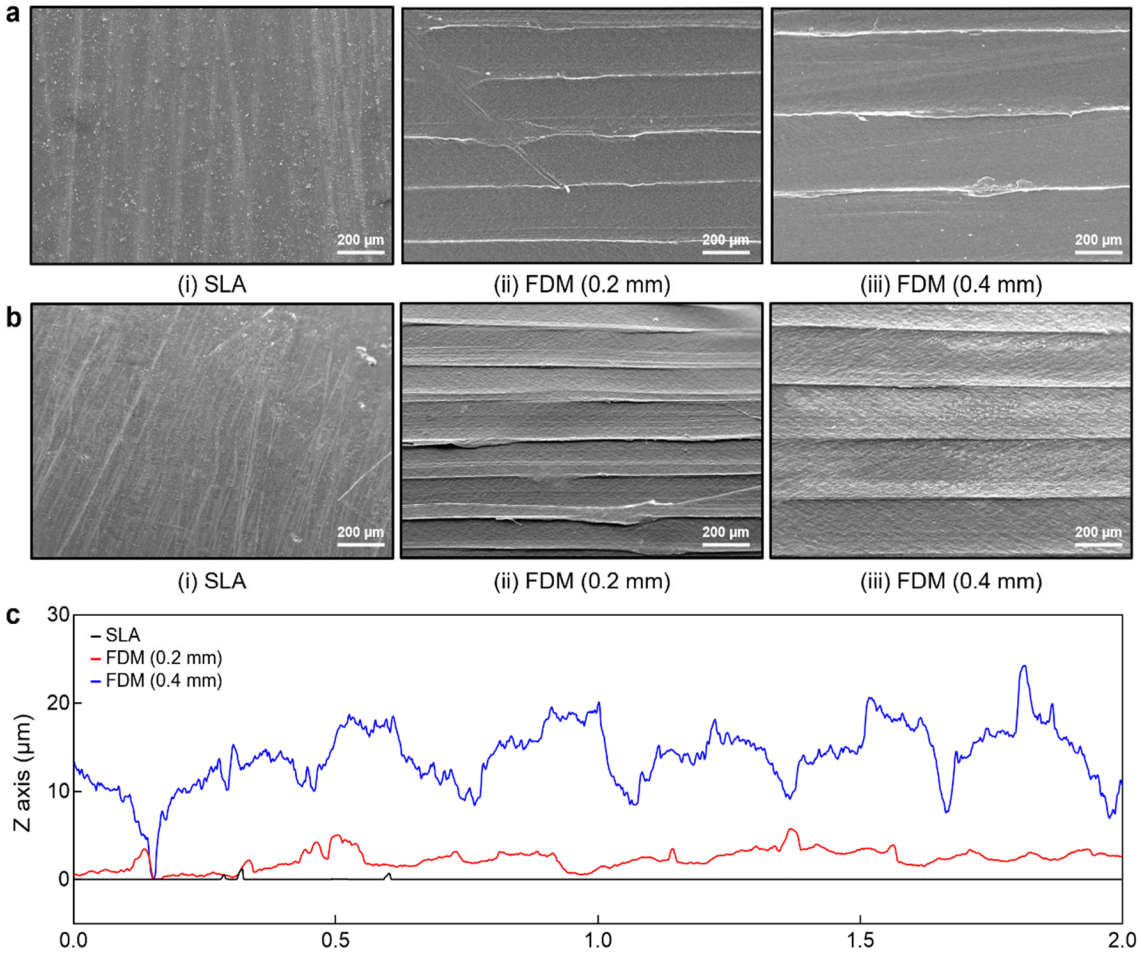

Figure 2. Surface morphology and topographical characterization of the 3D-printed master molds. (a) Top-view SEM images showing the surface finish of (i) SLA, (ii) FDM (fabricated with 0.2 mm diameter of nozzle), and (iii) FDM (fabricated with 0.4 mm diameter of nozzle) molds. (b) Tilted-view SEM images highlighting the three-dimensional topographical complexity and the stair-stepping effect inherently produced by the layer-by-layer deposition process in FDM. (c) Quantitative surface profiles demonstrating the increase in Z-axis topographical amplitude as a function of the programmed FDM nozzle, compared to the flat SLA control.

Abbreviations: FDM: Fused deposition modeling; SEM: Scanning electron microscopy; SLA: Stereolithography.

roughness ensured continuous analyte transport from the bulk flow to the enzyme-immobilized electrodes.

These theoretical predictions were corroborated by dye-mixing experiments (Figure 3d). In the SLA-based channel, the dye and clear solution remained distinctly separated, maintaining a sharp laminar interface even after navigating the serpentine path. While the 0.2 mm FDM channel exhibited marginal interface blurring, the limited step height was insufficient to generate the fluidic vorticity required for complete homogenization. In contrast, the FDM 0.4 mm channel achieved full homogenization, with the dye fully mixing into the clear medium before exiting the serpentine path. This dramatic shift in fluid behavior confirms that the surface artifacts inherent to FDM printing function as integrated passive micromixers.

3.3. Electrochemical characterization of the GOx and LOx sensors

The fundamental electrochemical behavior of the fabricated electrodes and the success of enzyme immobilization were initially evaluated using CV in 1 M PBS (pH 7.0) (Figure 4a–c). The characteristic capacitive current and the absence of significant redox peaks within the potential window (−1.0 V to 1.0 V) confirmed the electrochemical stability of the metal electrode. Following covalent enzyme immobilization via EDC/NHS chemistry, a noticeable alteration in the electrochemical signature was

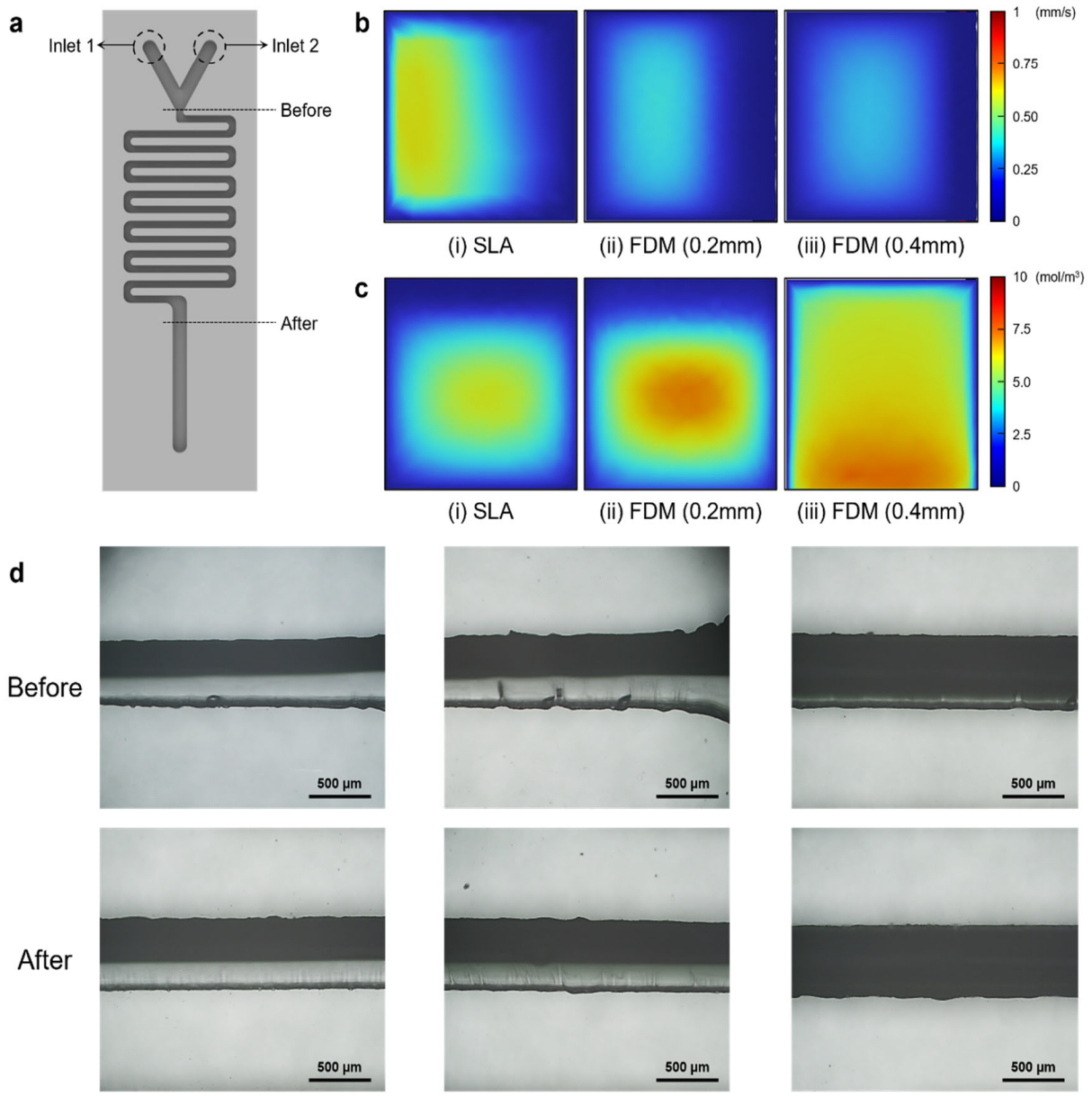

Figure 3. Numerical simulation and experimental validation of fluid dynamics and mixing mechanisms. (a) Schematic design of the serpentine microfluidic channel featuring dual inlets (inlets 1 and 2) and points "before" and "after" the serpentine mixing section. (b) Cross-sectional velocity profiles illustrating the flow distribution in (i) SLA, (ii) FDM (0.2 mm), and (iii) FDM (0.4 mm) channels. The FDM 0.4 mm model demonstrates superior velocity dispersion, effectively disrupting the stagnant boundary layer compared to the localized high-velocity core in the SLA control. (c) Concentration gradient simulations showing enhanced mass transport in the roughness-engineered channels. The FDM 0.4 mm channel achieves nearly uniform analyte delivery to the sensing interface, whereas the SLA model maintains a distinct depletion zone near the boundaries. (d) Experimental validation through dye mixing tests. Micrographs captured "before" and "after" the serpentine section reveal that the FDM 0.4 mm channel achieves complete homogenization through passive chaotic advection, while the SLA and FDM 0.2 mm channels retain visible laminar interfaces.
Abbreviations: FDM: Fused deposition modeling; SLA: Stereolithography.

observed (Figure 4b,c). A reduction in charging current and a slight shift in the potential envelope, relative to the bare Au electrode, indicated the successful formation of a protein layer on the electrode surface. This enzymatic layer acts as a partial passivation barrier to electron transfer at the electrode–electrolyte interface, verifying the effective grafting of biological recognition elements onto the active sensing areas.

The quantitative response of the sensors was assessed via chronoamperometry (CA), establishing a baseline sensitivity prior to integration into the microfluidic platform (Figure 4d). The stepwise current response of the sensors on the glass wafer was recorded following sequential additions of glucose and lactate at concentrations of 0.2, 0.5, 1.0, 2.0, and 4.0 mM. Upon analyte introduction, an increase in anodic current was observed at an applied potential of 0.1 V, corresponding to the electro-oxidation of hydrogen peroxide (H_2O_2) produced by the enzymatic reaction. In this non-microfluidic setup, the glucose sensor exhibited consistent sensitivity, confirming the functional activity of the enzyme-immobilized electrode interface.

Beyond sensitivity, biosensor specificity is critical for reliable monitoring in complex biological environments such as culture media (Figure 4e). Selectivity was evaluated against common electrochemical interferents, specifically ascorbic acid (AA) and uric acid (UA), at concentrations of 1, 2, and 4 mM. In the presence of both interferents, current fluctuations remained negligible relative to the robust signals produced by the target metabolic analytes. The resulting high signal-to-noise ratio supports the conclusion that enzyme–analyte specificity confers excellent selectivity under physiologically relevant conditions.

3.4. Enhanced sensing performance in FDM-based rough microfluidic channels

To verify that engineered surface roughness influences mass transport and sensing performance, real-time current responses for glucose and lactate were systematically compared across three experimental configurations: non-microfluidic, SLA-based smooth channels, and FDM-based rough channels (Figure 5). In the CA response of the glucose sensing channels, the FDM-based microfluidic channel exhibited a significantly higher and more distinct current step than the SLA channel upon sequential glucose addition (Figure 5a). This trend was even more pronounced in the lactate sensing profiles (Figure 5d). In both cases, the presence of micro-scale topographical features in the FDM channel led to an immediate and robust increase in anodic current, suggesting that the stair-stepping artifacts on the channel walls act as integrated passive mixers that facilitate the transport of analyte molecules to the enzyme-modified electrode surface. Unlike the smooth channel, the FDM-based configuration effectively leverages hydrodynamic perturbations to overcome diffusion-limited kinetics.

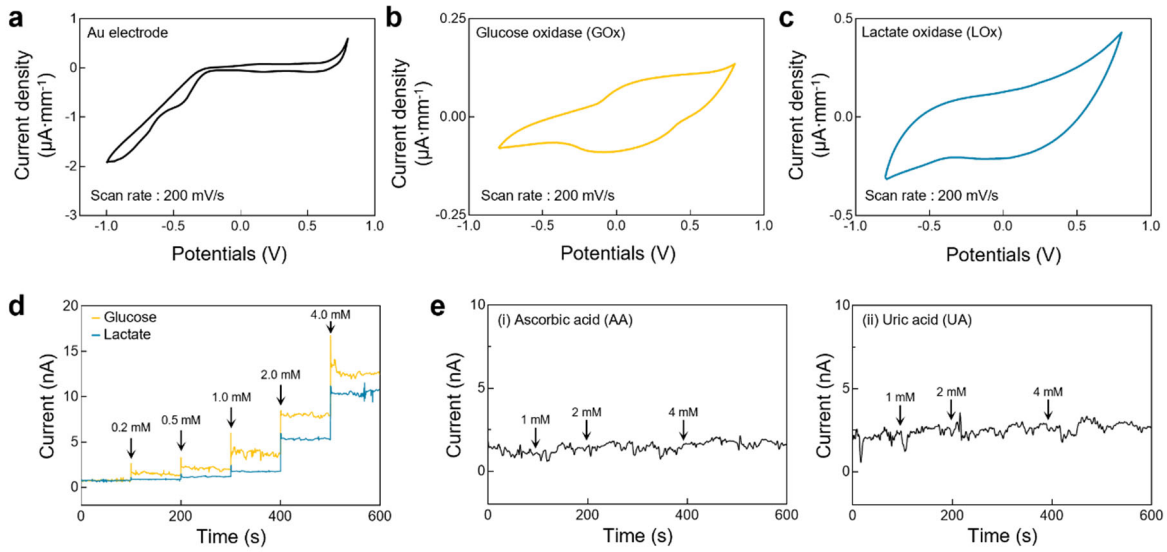

Figure 4. Electrochemical characterization and performance evaluation of the integrated biosensors. (a–c) Cyclic voltammetry (CV) profiles of the bare Au electrode (a), glucose oxidase (Gox)-immobilized electrode (b), and lactate oxidase (LOx)-immobilized electrode (c). (d) Amperometric response of the glucose (yellow) and lactate (blue) sensors upon sequential addition of analytes ranging from 0.2 to 4.0 mM. (e) Selectivity assessment against interfering analytes; (i) ascorbic acid (AA) and (ii) uric acid (UA). Negligible current fluctuations upon the addition of 1, 2, and 4 mM of interferents underscore the high specificity of the enzyme-immobilized electrodes for target metabolic flux monitoring.

The quantitative advantage of the FDM-based rough channel is further demonstrated through linear regression analysis of the sensitivity data. For glucose sensing, the FDM-based channel achieved a peak sensitivity of 6.983 ± 0.0335 nA/mM (Figure 5b,c), representing a substantial 36.8% improvement over the SLA-based smooth channel, which yielded 5.104 ± 0.139 nA/mM (Table S2). A consistent enhancement was observed for lactate sensing, where the sensitivity in the FDM-based rough channel reached 5.669 ± 0.0102 nA/mM, significantly higher than the 3.537 ± 0.0777 nA/mM measured in the SLA-based channel (Figure 5e,f, Table S2). This 60.3% increase in sensitivity underscores the effectiveness of engineered roughness in promoting analyte–electrode interactions.

In both cases, the presence of micro-scale topographical features in the FDM channel led to an immediate and robust increase in sensitivity, suggesting that the stair-stepping artifacts on the channel walls act as integrated passive mixers that enhance the delivery of analyte molecules to the enzyme-modified electrode surface. This improved sensitivity is particularly critical in applications involving 3D *in vitro* tissue models, where metabolic shifts must be tracked with high fidelity to accurately reflect the physiological state of the biological model.

3.5. Practical application with biomimetic hydrogel tissue phantoms

To evaluate the feasibility of the developed platform for monitoring analytes released from 3D *in vitro* tissue constructs, sensor performance was validated in a setup designed to mimic the metabolic microenvironment of a biological construct. This system enables real-time detection of analytes leaching from a porous 3D matrix, closely replicating the secretion profile of living tissues (Figure 6a). The configuration ensures that analytes released from the hydrogel are immediately captured by the flowing medium and transported to the sensing area (Figure 6b). SEM imaging revealed a highly interconnected microporous network essential for sustained diffusion of metabolic byproducts (Figure 6c). This porous architecture

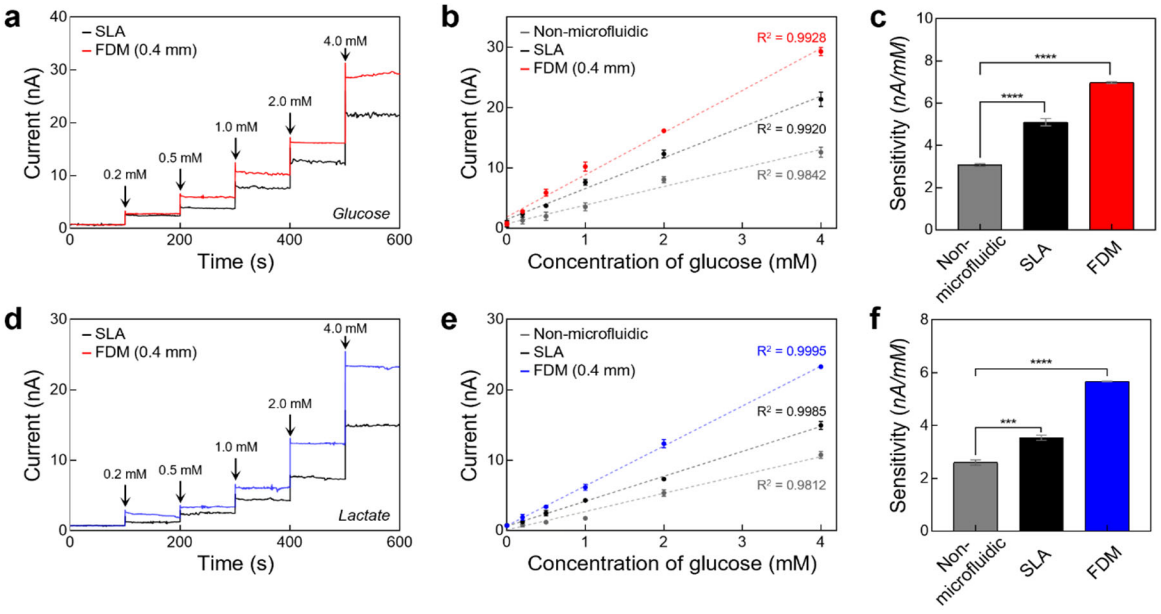

Figure 5. Quantitative comparison of electrochemical sensing performance across different channel topographies. (a–c) Glucose sensing evaluation: amperometric response to sequential glucose additions comparing SLA and FDM (0.4 mm) platforms (a); linear calibration for non-microfluidic, SLA, and FDM (0.4 mm) groups (b); and a sensitivity comparison bar chart highlighting the superior performance of the roughness-engineered FDM platform (c). The data were compared using a two-tailed unpaired Student's *t*-test: $n = 3$, $t(4) = 19.39$, $p < 0.0001$ (non-microfluidic vs SLA); $n = 3$, $t(4) = 89.45$, $p < 0.0001$ (non-microfluidic vs FDM 0.4 mm); where n is the number of samples. The data were presented as the mean ± standard deviation (SD) with $n = 3$, where n is the number of samples. $^{****}p < 0.0001$. (d–f) Lactate sensing evaluation: amperometric response to sequential lactate additions comparing SLA and FDM (0.4 mm) platforms (d); linear calibration for non-microfluidic, SLA, and FDM (0.4 mm) groups in lactate sensing (e); and a sensitivity comparison demonstrating consistent performance trends (f). The data were compared using a two-tailed unpaired Student's *t*-test: $n = 3$, $t(4) = 11.86$, $p < 0.001$ (non-microfluidic vs SLA); $n = 3$, $t(4) = 53.55$, $p < 0.0001$ (non-microfluidic vs FDM 0.4 mm); where n is the number of samples. The data were presented as the mean ± standard deviation (SD) with $n = 3$, where n is the number of samples. $^{***}p < 0.001$, $^{****}p < 0.0001$.
Abbreviations: FDM: Fused deposition modeling; SLA: Stereolithography.

allows the hydrogel to function as a reservoir, simulating the continuous efflux of glucose and lactate from 3D *in vitro* tissue models for assessment by the roughness-engineered sensing platform.

The real-time monitoring capability of the system was demonstrated by tracking the current response over an extended period of 500 min (Figure 6d). Upon flow initiation, three distinct groups, a control hydrogel (as-prepared), a glucose-loaded hydrogel, and a lactate-loaded hydrogel, exhibited a stable baseline current, confirming the absence of non-specific signals from the hydrogel matrix. The control hydrogel maintained a consistent baseline current even after loading into the microfluidic channels. In contrast, the glucose- and lactate-loaded hydrogels showed a progressive increase in anodic current as the analytes began diffusing from the matrix to the electrode surface. The high signal-to-noise ratio observed in these profiles enabled a clear distinction of metabolic signals from background noise.

In summary, the successful real-time monitoring of glucose and lactate from biomimetic hydrogel tissue phantoms validates the practical utility of the proposed platform as a robust tool for *in vitro* metabolic profiling. By achieving high sensitivity within a complex diffusion-based setup, the FDM-based microfluidic sensor demonstrates strong potential for integration with living 3D *in vitro* tissue models.

4. Conclusion

An electrochemically sensitive microfluidic sensing platform was developed by strategically repurposing the inherent surface roughness of FDM 3D printing as functional passive micromixers. Unlike conventional microfluidic fabrication methods that require complex, cleanroom-based processes, the integrated workflow using SLA and FDM printing offers a cost-effective, rapid prototyping solution for metabolic monitoring. Surface characterization confirmed that the stair-stepping artifacts in FDM-printed channels provide a deterministic and tunable topography absent in smooth SLA-based channels. Numerical simulations further elucidated the underlying mechanism, showing that these micro-topographical ridges induce localized vortices and transverse flow components that disrupt laminar streamlines and enhance analyte transport to the electrode surface. Experimental results demonstrated a significant enhancement in electrochemical sensing performance for both glucose

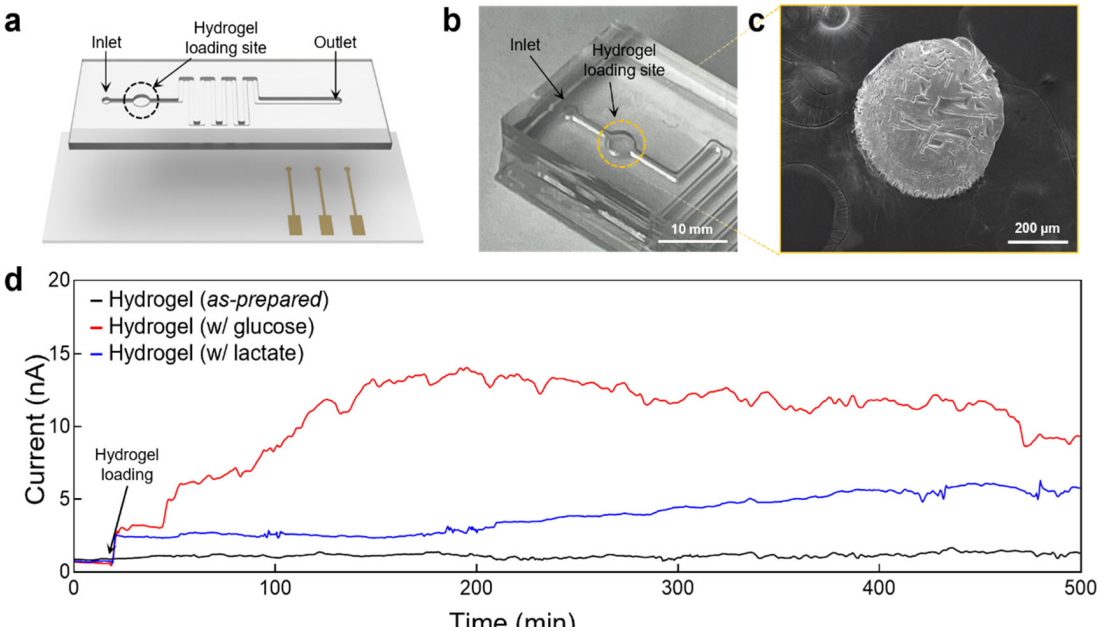

Figure 6. Real-time metabolic flux monitoring of biomimetic hydrogel phantoms for organ-on-a-chip applications. (a) Schematic illustration of the integrated microfluidic platform featuring a dedicated hydrogel loading site, serpentine mixing channel, and the underlying electrochemical sensing substrate. (b) Optical photograph of the fabricated PDMS-based microfluidic device, highlighting the chamber designed for the stable localized positioning of 3D tissue models. (c) SEM images of spherical hydrogel phantoms mimicking 3D *in vitro* tissues, such as spheroids or organoids. (d) Long-term amperometric monitoring of metabolic analytes over 500 min. The platform demonstrates the capability to capture distinct current profiles for glucose-loaded (red) and lactate-loaded (blue) phantoms upon loading, compared to the stable baseline of the as-prepared control (black).
Abbreviations: PDMS: Polydimethylsiloxane; SEM: Scanning electron microscopy.

and lactate. The FDM-based rough microfluidic channel achieved a glucose sensitivity of 6.983 nA/mM, representing a 127.4% and 36.8% improvement over non-microfluidic and SLA-based configurations, respectively. Similarly, the lactate sensor exhibited a high sensitivity of 5.669 nA/mM. These enhancements are directly attributed to improved mass transport driven by engineered surface roughness, which sustains a high concentration gradient at the enzyme-modified interface. Additionally, the FDM channels exhibited superior signal stability, a critical factor for detecting subtle metabolic fluxes in 3D *in vitro* tissue models. The practical utility of the platform was further validated through real-time monitoring of analyte release from biomimetic hydrogel tissue phantoms. The system successfully captured diffusion-limited kinetics of glucose and lactate over extended durations without significant signal degradation, demonstrating robustness for long-term physiological studies. By integrating low-cost 3D printing with high-fidelity electrochemical sensing, this work presents a high-performance diagnostic tool for *in vitro* metabolic profiling. This research highlights the potential to transform fabrication artifacts into functional design features, thereby enabling advanced disease modeling, drug screening, and personalized medicine, in which real-time metabolic data are paramount. Future work will focus on integrating multiple sensing modalities and enabling the direct culture of live 3D *in vitro* tissues within roughness-engineered microenvironments to further investigate cellular metabolic dynamics.

Acknowledgments

None

Funding

This research was supported by the Bio&Medical Technology Development Program of the National Research Foundation (NRF) funded by the Korean government (MSIT) (RS-2025-02243041); the National Research Foundation of Korea (NRF) grant funded by the Korean government (MSIT) (RS-2025-00557203); and the Basic Science Research Program through the National Research Foundation of Korea (NRF) funded by the Ministry of Education (RS-2025-25423539).

Conflict of interest

The authors declare no competing interests.

Author contributions

Conceptualization: Hyogeun Shin
Data curation: Giheon Kim
Formal analysis: Giheon Kim
Funding acquisition: Hyogeun Shin
Investigation: Giheon Kim
Methodology: Giheon Kim, Yeonghwa Hong, Seungjun Lee, Namsun Chou
Project administration: Hyogeun Shin
Resources: Namsun Chou
Supervision: Hyogeun Shin
Validation: Giheon Kim
Writing–original draft: Giheon Kim
Writing–review & editing: Giheon Kim, Hyogeun Shin

Ethics approval and consent to participate

Not applicable.

Consent for publication

Not applicable.

Availability of data

Data are available from the corresponding author upon reasonable request.

References

1. Cardoso, B.D., E.M. Castanheira, S. Lanceros-Méndez, and V.F. Cardoso. Recent advances on cell culture platforms for in vitro drug screening and cell therapies: from conventional to microfluidic strategies. *Adv. Healthc. Mater.* 2023;12(18):2202936.

   doi: 10.1002/adhm.202202936

2. Ko, J., D. Park, J. Lee, *et al*. Microfluidic high-throughput 3D cell culture. *Nat. Rev. Bioeng.* 2024;2(6):453-469.

   doi: 10.1038/s44222-024-00163-8

3. Dornhof, J., J. Kieninger, H. Muralidharan, *et al*. Microfluidic organ-on-chip system for multi-analyte monitoring of metabolites in 3D cell cultures. *Lab Chip*. 2022;22(2):225-239.

   doi: 10.1039/D1LC00689D

4. Nashimoto, Y., R. Mukomoto, T. Imaizumi, *et al*. Electrochemical sensing of oxygen metabolism for a three-dimensional cultured model with biomimetic vascular flow. *Biosens. Bioelectron*. 2023;219: 114808.

   doi: 10.1016/j.bios.2022.114808

5. Sun, C., G. Wu, D. Wu, *et al*. Determining the optimal transplantation window in hepatic organoids via real-time biosensing of vascularization and metabolic maturation utilizing the integrated organoid-on-a-chip platform. *Biosens. Bioelectron*. 2025:118057.

   doi: 10.1016/j.bios.2025.118057

6. Kim, Y., H. Kim, U.H. Ko, *et al*. Islet-like organoids derived from human pluripotent stem cells efficiently function in

the glucose responsiveness in vitro and in vivo. *Sci Rep*. 2016;6(1):35145.

doi: 10.1038/srep35145

7. Kim, J., J. Kim, Y. Jin, and S.-W. Cho. In situ biosensing technologies for an organ-on-a-chip. *Biofabrication*. 2023;15(4):042002.

doi: 10.1088/1758-5090/aceaae

8. Kim, Y., E.C. Chica-Carrillo, and H.J. Lee. Microfabricated sensors for non-invasive, real-time monitoring of organoids. *Micro Nano Syst. Lett*. 2024;12(1):26.

doi: 10.1186/s40486-024-00216-y

9. Lee, J., I. Soltis, S.A. Tillery, *et al*. Long-term stable pH sensor array with synergistic bilayer structure for 2D real-time mapping in cell culture monitoring. *Biosens Bioelectron*. 2024;254:116223.

doi: 10.1016/j.bios.2024.116223

10. Moya, A., M. Ortega-Ribera, X. Guimerà, *et al*. Online oxygen monitoring using integrated inkjet-printed sensors in a liver-on-a-chip system. *Lab Chip*. 2018;18(14):2023-2035.

doi: 10.1039/c8lc00456k

11. Weltin, A., S. Hammer, F. Noor, *et al*. Accessing 3D microtissue metabolism: Lactate and oxygen monitoring in hepatocyte spheroids. *Biosens. Bioelectron*. 2017;87:941-948.

doi: 10.1016/j.bios.2016.07.094

12. Heidenberger, J., E.I. Reihs, J. Strauss, *et al*. The effect of cyclic fluid perfusion on the proinflammatory tissue environment in osteoarthritis using equine joint-on-a-chip models. *Lab Chip*. 2025;25(9):2256-2269.

doi: 10.1039/D4LC01078G

13. Dupard, S.J., A.G. Garcia, and P.E. Bourgine. Customizable 3D printed perfusion bioreactor for the engineering of stem cell microenvironments. *Front Bioeng Biotechnol*. 2023;10:1081145.

doi: 10.3389/fbioe.2022.1081145

14. Ceccato, B.T., S.S. Vianna, and L.G. de la Torre. Numerical and experimental investigation of chaotic advection and diffusion mixing effects in 3D multihelical microfluidics for liposome synthesis. *Chem. Eng. Sci*. 2024;295:120190.

doi: 10.1016/j.ces.2024.120190

15. Fournié, V., B. Venzac, E. Trevisiol, *et al*. A microfluidics-assisted photopolymerization method for high-resolution multimaterial 3D printing. *Addit Manuf*. 2023;72:103629.

doi: 10.1016/j.addma.2023.103629

16. Nielsen, A.V., M.J. Beauchamp, G.P. Nordin, and A.T. Woolley. 3D printed microfluidics. *Annu Rev Anal Chem*. 2020;13(1):45-65.

doi: 10.1146/annurev-anchem-091619-102649

17. Wang, X., J. Liu, R. Dong, M.D. Gilchrist, and N. Zhang. High-precision digital light processing (DLP) printing of microstructures for microfluidics applications based on a machine learning approach. *Virtual Phys Prototyp*. 2024;19(1):e2318774.

doi: 10.1080/17452759.2024.2318774

18. Quero, R.F., B.M. de Castro Costa, J.A.F. da Silva, and D.P. de Jesus. Using multi-material fused deposition modeling (FDM) for one-step 3D printing of microfluidic capillary electrophoresis with integrated electrodes for capacitively coupled contactless conductivity detection. *Sens Actuator B-Chem*. 2022;365:131959.

doi: 10.1016/j.snb.2022.131959

19. Su, R., F. Wang, and M.C. McAlpine. 3D printed microfluidics: advances in strategies, integration, and applications. *Lab Chip*. 2023;23(5):1279-1299.

doi: 10.1039/D2LC01177H

20. Collingwood, J., K. De Silva, and K. Arif. High-speed 3D printing for microfluidics: Opportunities and challenges. *Mater Today Proc*. 2023.

doi: 10.1016/j.matpr.2023.05.683

21. Nelson, M.D., P.A. Tresco, C.C. Yost, and B.K. Gale. Achieving biocompatibility and tailoring mechanical properties of SLA 3D printed devices for microfluidic and cell culture applications. *Lab Chip*. 2024;24(19):4632-4638.

doi: 10.1039/D4LC00354C

22. Khoo, H., W.S. Allen, N. Arroyo-Currás, and S.C. Hur. Rapid prototyping of thermoplastic microfluidic devices via SLA 3D printing. *Sci Rep*. 2024;14(1):17646.

doi: 10.1038/s41598-024-68761-5

23. Shin, H., H.J. Lee, U. Chae, *et al*. Neural probes with multi-drug delivery capability. *Lab Chip*. 2015;15(18):3730-3737.

doi: 10.1039/c5lc00582e